Heat Transfer Conditions in Hydrogen-Fired Rotary Kilns for Iron Ore Processing

N.B. When citing this work, cite the original published paper.

(article starts on next page)

Article

Heat Transfer Conditions in Hydrogen-Fired Rotary Kilns for Iron Ore Processing

Elias Ehlmé,* Adrian Gunnarsson, Klas Andersson, and Fredrik Normann

Read Online

ACCESS | Metrics & More | Article Recommendations | Supporting Information

ABSTRACT: This work analyzes the heat transfer conditions in a rotary kiln used for the heat treatment of iron ore pellets in the grate-kiln process. The analysis concerns conditions relevant to fuel switching from coal to hydrogen gas. A modeling assessment of the radiative heat transfer in the kiln is conducted including the pellet bed and inner kiln wall temperature conditions. The results show that the heat transfer rate to the iron ore pellets under conditions of a pure hydrogen flame is comparable to the conditions relevant to coal firing. However, it is higher at the kiln wall surfaces near the burner region and lower in the remaining parts of the kiln. Increasing the particle concentration in the hydrogen flame represents a practical implication of co-firing coal with hydrogen. By adding particles, the emittance of radiation from the flame is significantly influenced, leading to further increased kiln surface temperatures closer to the burner position. Increased flame length also showed enhanced heat transfer rates to the kiln wall, although further away from the burner region.
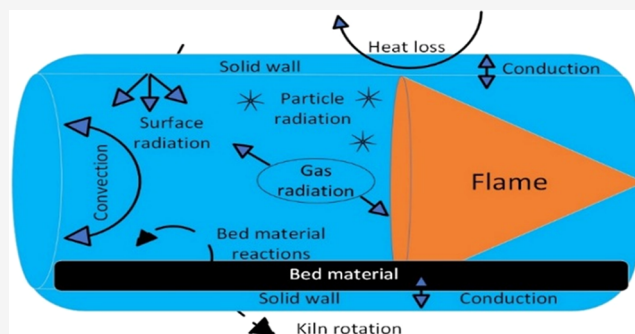
1. INTRODUCTION

The use of fossil fuels, for example in industrial heat treatment processes, leads to substantial carbon dioxide emissions. To lower these emissions, industrial users are examining the suitability of substituting their fossil fuels with renewable and/or decarbonized fuels, one alternative being hydrogen gas. One such industrial application is the iron ore grate-kiln process where a coal or oil-fired rotary kiln—a tilted, cylindrical, and rotating furnace—is applied for the heat treatment of a solid bed of iron ore.[1,2] While substituting coal (or oil) with hydrogen gas terminates emissions of carbon dioxide from the rotary kiln, it may, however, affect the heat treatment of the iron ore, possibly complicating the production of high-quality products, as well as the operational conditions of the kiln. It is, therefore, important to understand the heat transfer conditions within the kiln. Due to the large size and rotation of the kiln, the possibilities to conduct measurements are limited, and there is today a lack of knowledge regarding the current heat transfer conditions. It is therefore important to develop detailed modeling tools for accurate heat transfer predictions.

At high temperatures, such as in a kiln, radiation is more prominent and will hence be the dominating heat transfer mechanism. Complete substitution of coal for hydrogen eliminates char, ash, and soot particles from the flame. Also, there will be no carbon dioxide in the flue gas while the water vapor concentration will increase. These particles and gases have a large impact on the total heat transfer in the kiln as they absorb, emit, and scatter radiation.

The heat transfer conditions from coal and gaseous flames in cylindrical and rotating furnaces have been studied previously. Butler et al.[3] concluded, based on trials in a coal-fired laboratory-scale nonrotating cylindrical furnace, that coal and char particles are the main contributors to the heat flux to the wall surfaces. The particle radiation contribution has also been shown to dominate the total heat transfer in coal-fired pilot-scale kilns.[4,5] Thus, information regarding the temperature and the particle concentration distributions are more critical than gas concentrations when studying solid-fuel flames in order to predict radiative heat transfer. Such flames and heat transfer conditions have also been studied using various models. The work by Cross et al.[6] studied gaseous flame characteristics in a rotary kiln with gray radiative properties in a one-dimensional flame model, and they found that the model accurately predicted flame temperatures and radiative intensities. The convective heat transfer from the hot gas to the bed material and inner wall in an experimental kiln has been examined by Tscheng et al.[7] Conductive heat transfer has also been studied by several researchers, e.g., refs 8−10. Wes et al.[9] concluded from experimental measurements that the conductive heat
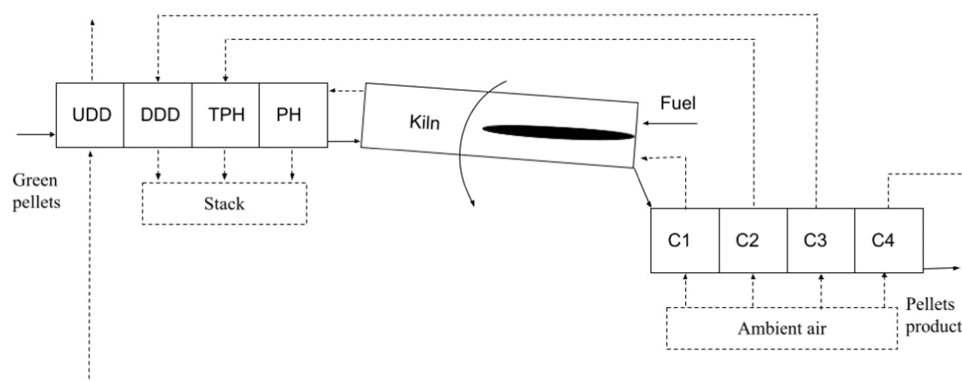
Figure 1. Schematic of the iron ore heat treatment in the grate-kiln process, including the grate zones: updraft drying (UDD), downdraft drying (DDD), temperate preheat (TPH), and preheat (PH), and the kiln as well as the cooler zones: C1−C4.
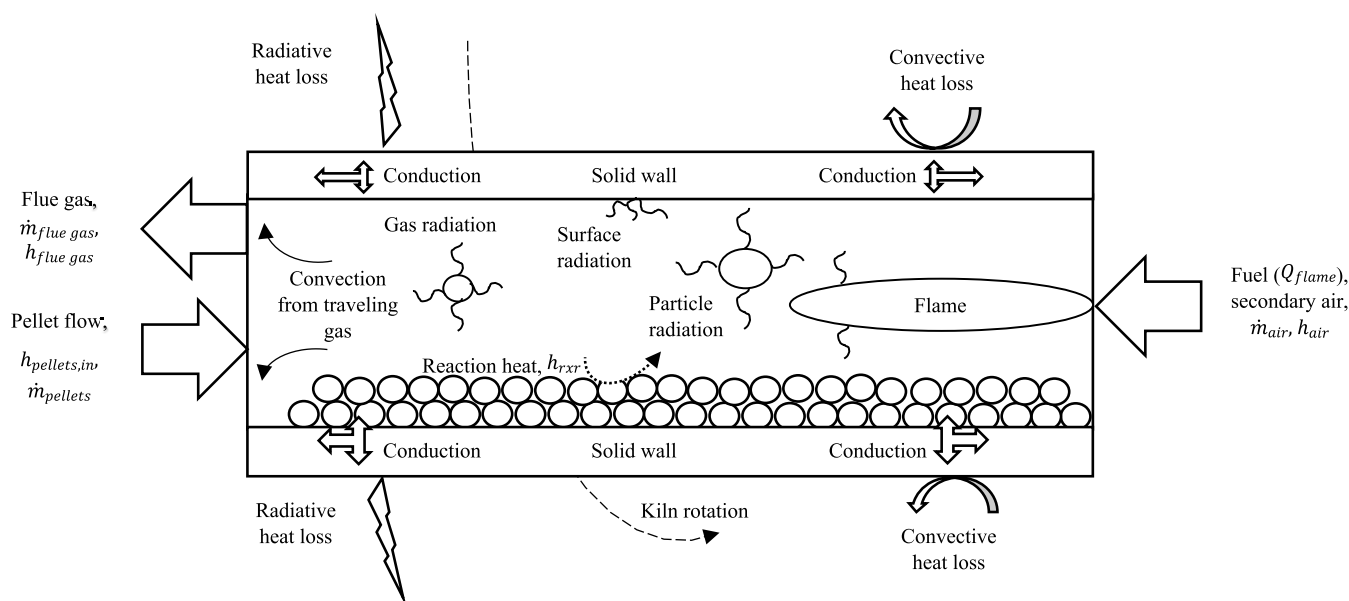

Figure 2. Schematic of a rotary kiln with a pellet bed and flame, showing the heat transfer mechanisms in the kiln.

transfer between the wall of a rotary drum reactor and its bed material can be described by penetration models, that is, mathematical models to describe the heat penetration through the material. Such models have been further studied by Li et al.[10] by developing an extended penetration model. Gorog et al.[11] developed a mathematical model to examine radiative, convective, and conductive heat transfer as well as the regenerative heat transfer from the rotating kiln wall. The radiative heat transfer from hydrogen flames has been studied with several radiation models in combination with developed submodels to account for gaseous radiation in, e.g., refs 12−15. However, studies of using hydrogen in rotary kilns at an industrial scale are scarce. In this work, the contributions of radiative heat transfer from particles and gases, as well as convective and conductive heat transfer are all examined in an in-house modeling tool of rotary kilns.

This work aims to map operational regimes relevant to a hydrogen-fired rotary kiln based on the heat transfer conditions, including the influence of flame length and presence of char particles. The findings are compared to the conditions in an industrial case of iron ore pelletizing, applying a coal flame.

2. METHODOLOGY AND MODELING

2.1. Grate-Kiln Process. Figure 1 illustrates the grate-kiln heat treatment process for the magnetite-rich iron ore studied. The iron ore is, mined, refined, and formed into so-called green pellets before entering the heat treatment process. During heat treatment, the pellets are dried, preheated, and oxidized from magnetite to hematite on a traveling grate, consisting of several zones, being updraft drying (UDD), downdraft drying (DDD), temperate preheat (TPH), and preheat (PH), zones.[1] The heat required to achieve appropriate process temperatures in these zones is supplied from hot streams of recycled air and flue gases from the downstream cooler section, zones C2−C4. After the grate, the pellets enter a rotary kiln where they are further heated, oxidized, and sintered by a large flame. The pellets are then cooled with ambient air in a cooler section, zones C1−C4. The outlet gas from cooler zone C1 is used as heated secondary air in the kiln. A more detailed description of the grate-kiln process for iron ore pellet induration can be found in the work of Jonsson et al.[1]

This work focuses on the heat transfer conditions within the rotary kiln for which Figure 2 illustrates the heat transfer mechanisms: radiation (gaseous and particles), convection,

and conduction. Operation of the rotary kiln aims to achieve a flame that extends far into the kiln and supplies an evenly distributed heat load to the bed material, as it is considered beneficial for the heat treatment process of the pellets as well as the pellet product quality.[4] A measure of pellet strength during the heat treatment process can be characterized by the pellet temperature-time history, an empirically determined function of temperature, and the duration time above a specified temperature threshold, specific to the heat treatment process. An example of modeled and measured pellet temperature distribution as a function of the distance from the feed in a coal-fired rotary kiln is presented in the work of Fan et al.[16]

2.2. Heat Transfer Model. The rotary kiln modeling tool used within this work has been developed in our previous work based on a full-scale kiln[17] and a pilot-scale kiln.[18] The model describes the heat transfer within the kiln, to the kiln inner surfaces, and to the pellet bed material, including radiation from the flame and kiln wall, convection from the warm gases, and conduction between the bed and wall, as illustrated in Figure 2. The heat of reaction from the exothermic oxidation of magnetite to hematite, Reaction R.1, obtained from Forsmo et al.,[19] is included as a source term in the model.

$$4\,Fe_3O_4 + O_2 \rightarrow 6\,Fe_2O_3 \quad \Delta H = (-119)\ kJ/mol$$

$$(R.1)$$
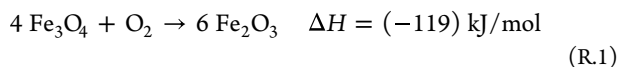
The model includes outer heat losses, as well as the movement of the kiln wall and bed material. The description of the rotation of the kiln is in accordance with our previous modeling work;[17] the portion of the bed material closest to the wall has a no-slip condition to the wall in the axial cross section but follows the wall with the rotation of the kiln. At a defined point, this part of the bed mixes with the bulk of the bed resulting in an average bed temperature. Thus, the bed material is divided into a surface layer and a bottom layer that move in the opposite directions of each other. The bottom bed layer that is in contact with the wall of the kiln is subject to conductive heat transfer, while the surface bed layer is subject to convective and radiative heat transfer. The model includes a simplified description of combustion but does not include fluid dynamics for gases within the rotary kiln. A more detailed description of the kiln model can be found in ref 17.

In summary, the heat transfer modeling tool solves the kiln energy balance, expressed in eq 1 and Figure 3, which includes
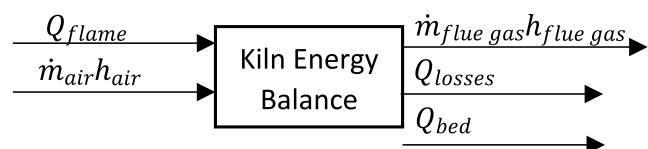
Figure 3. Kiln energy balance showing the energy in and out of a control volume.

the enthalpy change between the secondary air and flue gas, the heat losses from the kiln wall to the surroundings (Q_{losses}), the heat released from the combustion (Q_{flame}), and the heat transferred to the pellet bed via radiation, convection, and conduction (Q_{bed}). The energy balance of the bed is described by eq 2 and Figure 4, which includes the enthalpy change of the bed material, the sum of the heat generated by the exothermic oxidation reaction of the pellets, and the total heat transferred to the pellet bed. The modeling tool iteratively
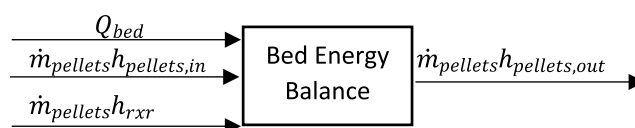
Figure 4. Bed energy balance showing the energy in and out of a control volume.

solves for the total heat transfer in the kiln, and the overall energy balance in eq 1 is, in turn, solved by iterating over the exit flue gas temperature, as shown in the method of solution scheme (Figure 5). The simulation is considered converged at an error margin of below 1%.

$$Q_{flame} = \dot{m}_{flue\ gas}h_{flue\ gas} - \dot{m}_{air}h_{air} + Q_{losses} + Q_{bed} \quad (1)$$

$$\dot{m}_{pellets}(h_{pellets,out} - h_{pellets,in}) = \dot{m}_{pellets}h_{rxr} + Q_{bed} \quad (2)$$
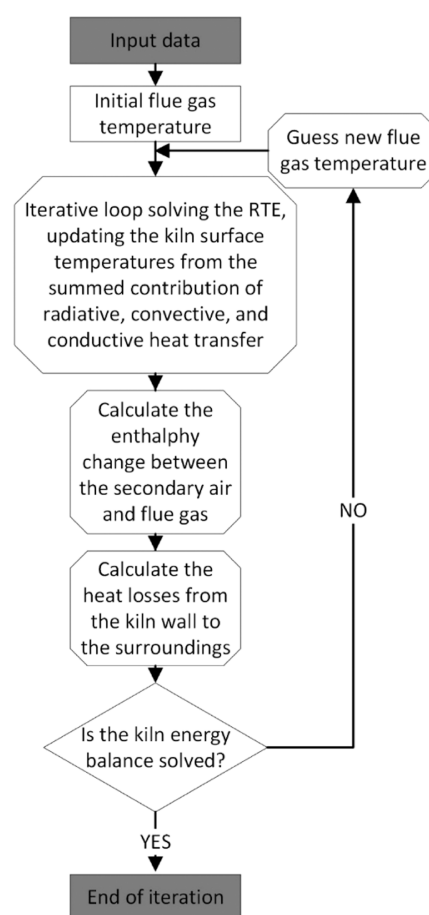
Figure 5. Overall method of solution of the model.

2.2.1. Radiative Heat Transfer Equation and Submodels. As radiation dominates the total heat transfer in the kiln, the modeling tool is built around the radiative heat transfer equation (RTE), expressed in eq 3, which for a given wavenumber v describes the change in radiative intensity from the summed contributions of absorption, emission, and scattering along a set direction, $\hat{s}$.[20] The absorption coefficient κ_v is dependent on the gases and particles present. The scattering of thermal radiation is dependent on the particles present only and defined by the scattering coefficient σ_s. The integral term describes the spectral intensity that is scattered

Table 1. Cases Studied with the Modeling Tool Including the Model Inputs

case nr:	case specification	parameter studied	temperature input	gas concentration input	particle concentration input
(reference)	11.4 m coal flame		adiabatic	H_2O, CO_2	char, soot
0	5.4 m hydrogen flame		adiabatic	H_2O	
1	3.4 m hydrogen flame	flame length	adiabatic	H_2O	
2	11.4 m hydrogen flame	flame length	adiabatic	H_2O	
3	23.5 m coal flame	flame length	adiabatic	H_2O, CO_2	char, soot
4	5.4 m hydrogen flame with added coal particles corresponding to 2% of the surface area in a 5.4 m reference coal flame	particle radiation	adiabatic	H_2O	char
5	5.4 m hydrogen flame with added coal particles corresponding to 5% of the surface area in a 5.4 m reference coal flame	particle radiation	adiabatic	H_2O	char

from the direction $\widehat{s_i}$ into direction $\hat{s}$ as a function of the scattering phase function, Φ_ν, and a solid angle, $d\Omega_i$. The scattering phase function describes the probability of scattering a ray from $\widehat{s_i}$ into the $\hat{s}$ direction.

$$\frac{dI_\nu}{ds} = \kappa_\nu I_{b\nu} - \kappa_\nu I_\nu - \sigma_{s\nu} I_\nu + \frac{\sigma_{s\nu}}{4\pi} \int_0^{4\pi} I_\nu(\widehat{s_i})\Phi_\nu(\widehat{s_i}, \hat{s}) \, d\Omega_i \tag{3}$$

A discrete-ordinates method (DOM) that approximates the solution is used in this work to solve the RTE. The rotary kiln is divided into three-dimensional cells, in the radial, axial, and angular directions, which may store values of temperature, concentration, and radiative properties for both particles and gases. In this study, the model uses a cell resolution of 30 × 300 × 96 in the axial, radial, and angular directions, as the model proved to be more or less grid-independent at this resolution. The incident radiative heat flux to the wall and bed material is calculated from the radiative intensity for a set of weighted discrete directions for each cell. The directions used are derived according to an S_8 approximation from the work by Tsai et al.[21] The kiln wall and iron ore pellets are treated as gray bodies with an emissivity of 0.9, and the pellets are considered lying as a bed, exchanging radiation. Given a set of input data, the RTE is iteratively solved within the modeling tool, applying the DOM for each cell. All bed and wall temperatures are then updated from the contributions of flame, bed and wall radiation, convection, and conduction, starting at the inlet position of the bed material at the first axial cell. As outputs from the model, bed and wall temperature profiles as well as the quantified contribution from radiation, convection, and conduction to the bed are obtained. In this work, the input data of temperature and gas concentration profiles were calculated from the adiabatic flame temperature, whereas data of particle concentration are based on measurements from experimental campaigns,[5] as is described in more detail below.

2.2.1.1. Submodels. The heat transfer model assumes an overall gray intensity, using gray coefficients to represent the contributions of gases and particles, thus simplifying the RTE. For each cell in the model, the gray gas absorption coefficients are estimated using a weighted sum of gray gases (WSGG) model in which the absorption coefficients are functions of the gas temperature and concentrations of H_2O and CO_2. In this work, two different WSGG models are used, each with a set of four gray gases and one clear gas. For hydrocarbon flames, coefficients derived from the work of Johansson et al.[22] are applied. For a hydrogen gas flame, no carbon dioxide is formed, and parameters from the work of Bordbar et al.[23] are applied, specified for a gas containing water and transparent gas only. The parameters are specified for temperatures up to

2400 K in the existing models, and, since flame peak temperatures are expected to surpass this limit for a hydrogen flame since preheated air is used as an oxidant, the model is constant over 2400 K in those computational cells.

The modeling of the radiative heat transfer also includes the radiative properties of the different present particles. Therefore, Rayleigh theory is applied to describe the particle radiation of soot particles by calculating the absorption coefficient using a volume fraction, and Mie theory to simulate the particle radiation of fuel, and ash particles using a particle size distribution. The complex refractive indices for soot particles are gathered from Chang and Charalampopoulos.[24] The indices for fuel particles are gathered from Foster and Howarth[25] and for ash particles a combination of the work from Lohi et al.,[26] Gupta and Wall,[27] and Goodwin and Mitchner.[28] The spectral properties may be transformed into gray particle properties by means of Planck averaging, and then be used together with the WSGG model to solve the RTE.

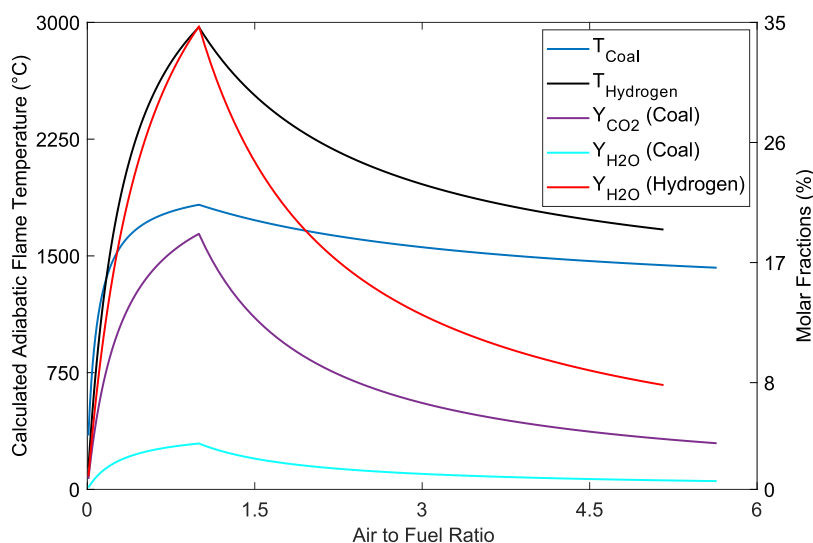**2.3. Reference Settings, Cases, and Data Inputs.** *2.3.1. Reference Settings.* The total heat transfer under conditions of a hydrogen flame is related to a set of reference settings, which mimics the conditions of an industrial rotary kiln heated with a coal flame, by altering a set of parameters in the modeling tool. The reference case is based on a commercial-scale kiln that measures 2.66 m in radius and 33.3 m in length and includes some input parameters that are kept constant between cases being: Bed temperature entering the kiln is 1000 °C, the gas temperature fed to the kiln (secondary air) is 1200 °C, a 16–17% oxygen concentration in the flue gas, the feeding rate of the pellets (~153 kg/s), and the thermal energy from the fuel is 35 MW. Kiln operating conditions of rotational speed and the angle of inclination are 2 RPM and 3 degrees, respectively. The inclination is integrated in the feeding rate of the pellets, and both of these parameters affect the residence time of the iron ore pellets in each computational cell. As such, these parameters are maintained constant in this work.

2.3.2. Process Conditions. The process conditions studied including the input parameters when using the modeling tool are presented in Table 1. The reference coal flame is specified with a flame length of 11.4 m, as obtained from the work of Gunnarsson et al.,[17] and the pure hydrogen flame, Case 0, is specified to 5.4 m, hypothesized by the reactivity and physical properties of hydrogen.

From observations and experiences at commercial-scale conditions, the flame length may vary in size, especially when shifting fuels. Thus, the effect of the flame length on radiation, convection, and conduction to the kiln surfaces was studied for hydrogen and coal in Cases 1–3.

Table 2. Data Input of the Particle Concentration of Char Particles Listed as the Total Projected Surface Area in the Kiln, and the Volume Fraction of Soot Particles for the Reference Coal Flame and Case 3

char concentration: coal flame		soot concentration: coal flame	
11.4 m flame length: 28.6×10^{-2} $[m^2_{char\ particles}/m^3_{air}]$	23.5 m flame length: 52.1×10^{-2} $[m^2_{char\ particles}/m^3_{air}]$	11.4 m flame length: 3.74×10^{-9} $[m^3_{soot}/m^3_{air}]$	23.5 m flame length: 3.58×10^{-9} $[m^3_{soot}/m^3_{air}]$

Figure 6. Adiabatic flame temperature of hydrogen (black line) and coal (blue line), as well as the respective molar fractions of water vapor and carbon dioxide, as a function of their respective air-to-fuel ratios.

Char particles representing unburned fuel in coal combustion are added to the hydrogen flame in Cases 4 and 5 to examine the possibility of enhancing radiative heat transfer to the kiln surfaces. Different particle concentrations corresponding to a fraction of the available particles in a pure coal flame were studied for a hydrogen flame, representing hydrogen and coal co-firing. The hydrogen fuel is assumed to undergo complete combustion while added particles are inert and radiating.

2.3.3. Cases. 2.3.3.1. Data Input: Particle Concentrations. The set of data inputs in this work include particles of char and soot, which are considered for the coal flames; ash particles are not considered as they were found to be present to a much lower degree in ref 5. Particles are not considered for the hydrogen flames, with the exception in Cases 4 and 5, in which only char particles were included.

Total concentrations of char particles and soot in the kiln for the coal flames are presented in Table 2 as a total value for the entire kiln volume and are based on measurements from an experimental campaign conducted in a pilot-scale kiln.[5] In that study, the thermal input of fuel was 580 kW using the same fuel that is used in the industrial scale rotary kiln as well as in this work. In the model, each particle type is, as a simplification, represented by stationary inert spheres with a representative particle diameter, and the concentration of particles along the furnace axis at specific fractions of the flame length was determined by fitting it to radiative intensity measurements in ref 5. Here, the radiation from the char particles is accounted for in the form of a projected surface area. The radial distribution of particles is assumed to follow a cosine profile along the furnace diameter with a peak value at the centerline of the kiln, as done in previous work.

Soot particles are introduced as a volume fraction of a computational cell occupied by soot. Again, cosine profiles were adopted to consider the distribution and decay of the soot volume fractions outside the measurement region. How the soot volume fractions are defined is described in detail from measurements on propane flames in the Chalmers 100 kW test facility.[29]

2.3.4. Flame Temperature and Gas Concentration Profiles. To define the temperature and gas concentration profiles required as input data to the heat transfer model, a mixing function for how the secondary air stream is considered to be mixed with fuel along the kiln axis within the modeling tool is defined in eq 4. The function assumes the flame to widen as a cone (R_{flame,n_z}) inside the kiln from being only fuel at the burner outlet to being perfectly mixed with secondary air at a specified flame length ($R_{flame,n_z} = R_{kiln}$).

$$\lambda_z = \frac{R_{flame,z}^2}{R_{kiln}^2} \lambda_{max} \tag{4}$$

To describe the conditions along the axial centerline of the flame, the calculated air-to-fuel ratio is correlated to the adiabatic flame temperature of the applied fuel, as illustrated in Figure 6. Figure 6 includes a coal flame implemented with the fuel-specific data as presented in Table 3 and a hydrogen flame as pure hydrogen gas as well as the respective gas concentration of water vapor and carbon dioxide. For reference, the measured peak in-flame temperature during the pilot-scale trials with coal was around 1600 °C, i.e., 225 °C lower than the adiabatic flame temperature, see ref 5.

The air-to-fuel ratio (λ_z) in the center ($n_r = 1$) of the flame cone is assumed proportional to the ratio between the flame and kiln cross-sectional areas as well as λ_{max}, as expressed in eq 4. The temperature of the cells along the cone centerline is set as the adiabatic flame temperature corresponding to coal or hydrogen fuel and the calculated air-to-fuel ratio of each axial cell position of the flame cone (n_z), according to eq 5 and Figure 6. Here, n_r is the radial position of the flame cone.

Table 3. Composition of the Coal Fuel Gathered from Ref 30

component	coal
moist [mass-%]:	1.40
ash [mass-%]:	13.6
C [mass-%]:	75.5
H [mass-%]:	4.2
N [mass-%]:	1.35
O [mass-%]:	5.00
S [mass-%]:	0.34
sum:	101.4
Lower Heating Value [MW/kg] Coal	
29.3	

$$T(n_r = 1, n_z) = f(\lambda_z) \tag{5}$$

For each axial position (n_z), the flame cone is divided into several flame layers (n_{flame}) in the radial direction, with each layer thickness corresponding to the width of a cell in the radial direction. Also, for each axial position, the temperature profile is assumed to be radially symmetric. The temperature in each flame layer is determined from eq 6 in which the temperature is assumed to decrease linearly from the adiabatic flame temperature at the flame center $(n_r = 1)$ in accordance with eq 5. In this way, the adiabatic flame temperature of the fully mixed gases is obtained at the outer boundary of the cone $[T(n_{flame}, n_{z,max}) = f(\lambda_{max})]$, resulting in a linear radial temperature decrease.

The preheated air also follows a temperature profile, where $T_{air,in} = 1200$ °C increases linearly toward the flame cone boundary temperature in the axial direction, as expressed in eq 7. The number of axial positions occupied by the air from the kiln inlet to the flame cone boundary $n_{r,max}$ is identified as $n_{z,air,max}$. Figure 7 illustrates an example of the flame cone divided into four radial positions.

$$T(n_r, n_z) = T(n_r = 1, n_z)$$
$$+ \frac{T(n_{flame}, n_{z,max}) - T(n_r = 1, n_z)}{n_{flame} - 1}(n_r - 1) \tag{6}$$

$$T_{air}(n_{r,air}, n_{z,air}) = T_{air,in} + \frac{T(n_{r,max}, n_z) - T_{air,in}}{n_{z,air,max} - 1}(n_{z,air} - 1) \tag{7}$$

At subsequent axial positions, the air-to-fuel ratio and the adiabatic flame temperature are updated according to eqs 4 and 5, resulting in as many linear temperature profiles as there are axial positions within the flame. Together, the linear

temperature profiles construct a flame temperature map, which is used as input data in the model. A similar procedure is conducted to define the gas concentration map of the flame, but by using the fuel and air-to-fuel ratio derived molar fractions of water vapor (and carbon dioxide) in Figure 6 to define the centerline. In the secondary air, water vapor and carbon dioxide assume a molar fraction of 0.01 each.

2.3.5. Temperature Conditions. The calculated temperature conditions in the form of a contour map are illustrated in Figure 8a for the reference case; the color-coded cells represent the upper half of the horizontal cross section of the kiln. Similar temperature contour maps as well as gas concentration maps of water vapor and carbon dioxide were obtained for all of the studied cases. For the corresponding profiles of the reference coal flame and Case 0, see the Supporting information: Data input of the carbon dioxide and the water vapor concentration for the reference coal flame (S1), as well as the input of the temperature profile and the water vapor concentration for Case 0 (S2).

To compare with measurements, Figure 8b presents the temperature input data, showing the bottom half of a horizontal cross section of the kiln of an 11.4 m coal flame, constructed from five radial temperatures, measured in three positions along a pilot-scale test furnace gathered from ref 5. The temperatures are scaled to fit the same full-scale kiln used in this work and linearized between the cells to define a temperature map over the kiln. The main difference between Figure 8a,b is the assumed flame shape and the temperature of the secondary air (1200 °C compared to 1100 °C). The calculated peak flame temperature at 1825 °C is higher than what was measured, being about 1600 °C. Therefore, it is of interest to simulate nonadiabatic cases as well; thus, the peak flame temperature in the hydrogen flame of 2960 °C was decreased with a corresponding peak temperature difference of 225 °C between the modeled (Figure 8a) and measured (Figure 8b) coal flames. That is, all computational cells kept their temperature but a maximum boundary of 2735 °C was introduced to reduce the peak temperatures. However, since the majority of the gas volume remained unaffected, the result from this simulation showed only a small difference in the heat transfer conditions of this nonadiabatic hydrogen flame compared to Case 0.

3. RESULTS AND DISCUSSION

Table 4 presents the calculated heat transfer conditions in the rotary kiln for the reference 11.4 m coal flame and the 5.4 m hydrogen flame (Case 0). Additional cases for coal and hydrogen where the gas temperature is maintained at 1200 °C in the cells closest to the kiln wall and bed material,
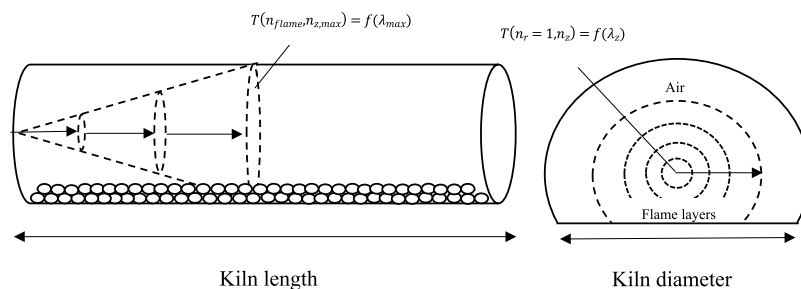

$T(n_{flame}, n_{z,max}) = f(\lambda_{max})$

$T(n_r = 1, n_z) = f(\lambda_z)$

Air

Flame layers

Kiln length

Kiln diameter

Figure 7. Schematic of the flame cone, and an example of the discretization of the flame where the flame length inside the kiln is divided into three axial positions (left) and the flame diameter (dashed) divided into four radial positions (right).
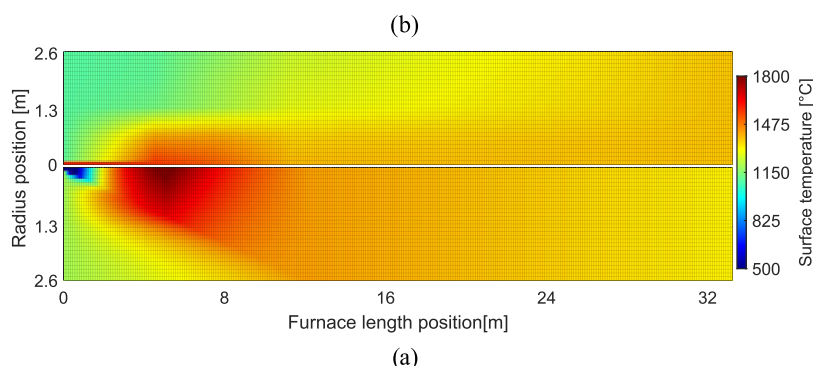
Figure 8. (a) (Bottom): Data input (with grid) of the temperature profile for the reference 11.4 m coal flame with a flue gas temperature of 1323 °C and (b) (top) for an 11.4 m coal flame based on measurements from pilot-scale tests[5] (flue gas temperature of 1300 °C).

Table 4. Calculated Heat Transfer Conditions for the Reference Coal Flame, Case 0, and a Coal and Hydrogen Case Where the Gas Temperature Is Maintained at 1200 °C in the Cells Closest to the Kiln Wall[a]

heat transferred to the bed (MW)	11.4 m coal flame (reference)	5.4 m hydrogen flame (Case 0)	11.4 m coal flame with gas temperature at 1200 °C closest to kiln wall and bed	5.4 m hydrogen flame with gas temperature at 1200 °C closest to kiln wall and bed
radiation	19.8	18.6	20.2	18.9
convection	3.00	4.80	1.10	1.10
conduction	1.20	1.10	1.20	1.10
sum	23.9	24.5	22.5	21.2
outlet product temperature [°C]	1250	1255	1239	1229
flue gas temperature [°C]	1323	1344	1352	1394

[a]The sum of radiation convection and conduction corresponds to the heat transferred to the bed.
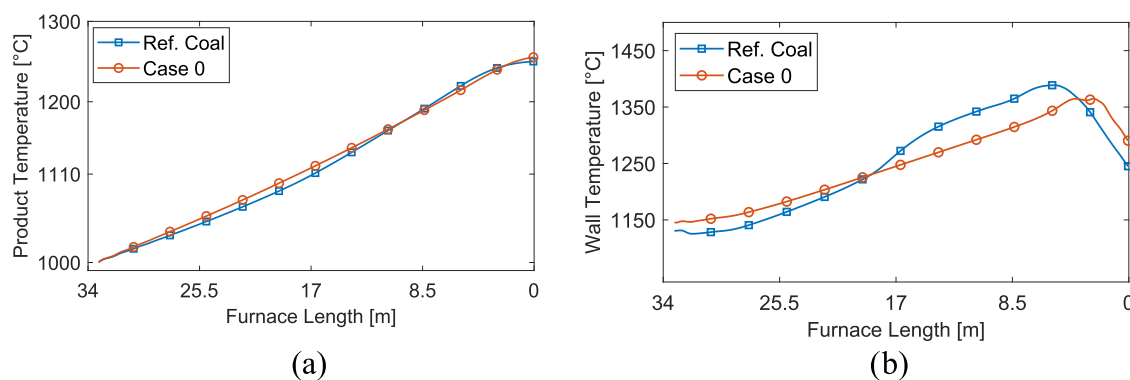

Figure 9. Surface temperature profiles for reference coal flame and Case 0 for the (a) bed material and (b) kiln wall.

corresponding to the secondary gas temperature, are included. The calculated outlet product and flue gas temperature of Case 0 are higher than the coal reference flame. Case 0 shows an increased total heat transfer to the bed by 0.6 MW relative to the reference flame. The shorter flame in Case 0 increases gas temperatures in the later parts of the kiln, which enhances convective heat transfer to the bed in comparison to the reference case. Additionally, the lower radiative heat transfer in Case 0 reduces the wall temperature and, in turn, the conductive heat transfer between the kiln wall and the bed. The cases with constant gas temperature at 1200 °C in the cells closest to the kiln wall illustrate the importance of convective heat transfer for the increased heat transfer of Case 0. The analysis shows a similar contribution from convective heat transfer between the coal and hydrogen cases, but a significant decrease in convective heat transfer between the hydrogen case and Case 0. This is due to the lower temperature gradient between the gas and kiln surfaces.

Mixing and avoiding gas layering along kiln surfaces could, thus, enhance the total heat transfer from the hydrogen flame.

3.1. Reference Coal and Hydrogen Kiln Temperature Profiles. The calculated kiln surface temperatures, including the inner kiln wall and the product, for the reference coal flame and Case 0, are illustrated in Figure 9a,b, respectively. The product temperature profile between the reference and the hydrogen flame, Case 0, in Figure 9a, shows that inertia exists in the product bed material that can handle the fuel shift in the process why the change in product temperature is modest. However, local wall temperatures are significantly affected between cases. As observed in Figure 9b, Case 0 holds higher temperatures in the peak flame temperature region, 0−4 m from the burner along the furnace length, compared to the reference. Figure 9b also shows decreased temperatures for Case 0, between 4 and 18 m, compared to the reference case due to the absence of particles.

3.2. Heat Transfer Conditions. The product bed temperature at the kiln outlet for the reference coal flame and Cases 0−5 are presented and discussed in the sections below. The calculated heat transfer conditions for Cases 1−5 in relation to the reference coal flame are presented in Table 5, and the results are discussed in subsequent sections. For the corresponding values of the reference, and Case 0, see Table 4.

Table 5. Calculated Heat Transfer Conditions for Cases 1−5 Relative to the Reference Coal Flame

heat transferred to the bed relative to the reference coal flame (%)	case 1	case 2	case 3	case 4	case 5
radiation	90	106	126	102	111
convection	165	149	71	157	153
conduction	89	99	120	97	103
total heat transferred to the bed	100	111	119	108	116

3.2.1. Flame Length. The flame length affects the radiative heat transfer within the kiln since it affects the volume of hot gases (and particles) as well as the positioning of the peak in wall temperature, as is observed in Figure 10. An increase in hydrogen flame length, Cases 0−2, effectively enhances radiative heat transfer by water vapor to the kiln surfaces as a larger gas volume is allowed for an increased temperature, see Figure 10a. Consequently, a reduced convective heat transfer is achieved due to the extended time to reach plug flow, which creates a lower temperature gradient between the kiln wall and passing gas flow. In the presence of particles, a longer flame (Case 3) results in an overall higher concentration of particles in the kiln and increases the heat transferred to kiln surfaces as well, see Figure 10b.

3.2.2. Particle Radiation. Figure 11a gives the wall temperatures of Cases 4 and 5—the same temperature and gas composition inputs as for Case 0, but with increased particle concentration. The introduction of particles increases peak temperatures in the wall close to the burner inlet and significantly enhances heat transfer to the kiln surfaces via radiation. The observed elevated wall temperatures may impose significant thermal stresses on the kiln, which may not be favorable. Additionally, Figure 11a indicates that Cases 4 and 5 maintain higher kiln wall temperatures up to approximately 8 m from the burner inlet, compared to the reference.

The progress of the radiative, convective, and conductive heat transfer from the hydrogen flame to the product as a function of particle concentration (0−5%) is presented in Figure 11b, illustrating that the effect of particle radiation in relation to convective and conductive heat transfer to the product is modest. However, Case 5 shows an increased radiative heat transfer to the product bed material by 3.3 MW compared to Case 0. Furthermore, Table 5 also shows that the radiative heat transfer in Case 5 is enhanced compared to the reference coal flame, and the convective heat transfer is higher due to the higher gas temperatures yielding a higher product temperature leaving the kiln, see Figure 11c. In summary, introducing higher particle loads to the hydrogen flame significantly affects the kiln wall compared to the product. Increased particle loads enhance radiative heat transfer to the kiln surfaces, resulting in elevated wall temperatures. Consequently, this reduces the temperature gradient between the kiln surfaces and the hot gases, resulting in a proportional decrease in convective heat transfer. Furthermore, at the higher peak temperatures of the hydrogen flame, the particles absorb and emit significantly more radiation than the reference coal flame, that is why relatively low concentrations of particles have a high effect on the kiln surfaces, as seen in Figure 11a,c.

4. DISCUSSION

4.1. Future Modeling Work. The utilized prescribed flame lengths, particle concentration, and linearized temperature and gas composition profiles based on adiabatic conditions result in uncertainties. Since there is a lack of available detailed data regarding the temperature from industrial hydrogen/co-firing flames, the usage of prescribed data inputs offers the availability to isolate the effect of temperature conditions on heat transfer and the kiln energy balance under industrial conditions for various fuel and firing scenarios. Applying the heat transfer model for process design requires, therefore, further development. Future work should aim to evaluate the representation of the temperature and gas composition under conditions of hydrogen firing through combinations of experiments and computational fluid dynamics. Additionally, particle profiles can be assessed through experiments.

It should be noted that the model is based on the radiative heat transfer equation, which includes detailed submodels for particles and gaseous radiation modeling. The submodel for convective heat transfer is less developed in the current model, resulting in larger uncertainties and requiring further development. Lastly, evaluating the impact of kiln wall temperature and how the resulting heat load affects the kiln and pellet bed
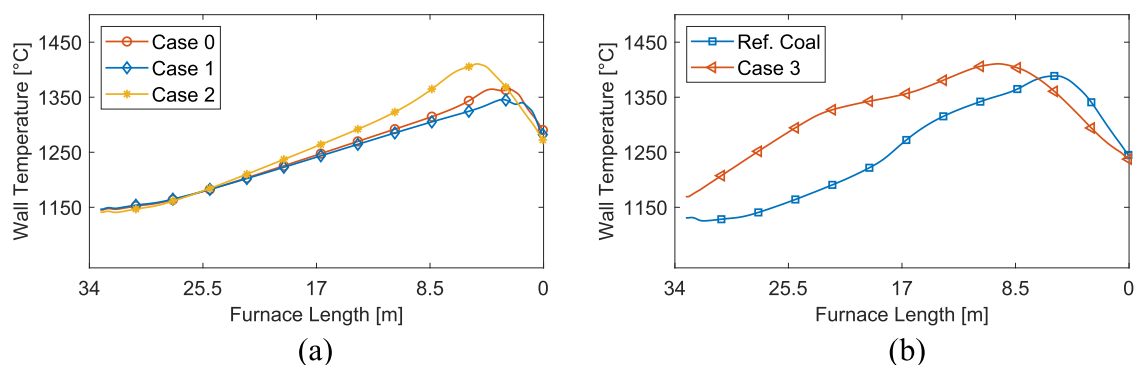

Figure 10. (a) Kiln wall temperature profiles for Cases 0−2. (b) Kiln wall temperature profile for the reference coal flame and Case 3. The flue gas temperatures for Cases 1−3 are 1354, 1313, and 1266 °C, respectively.
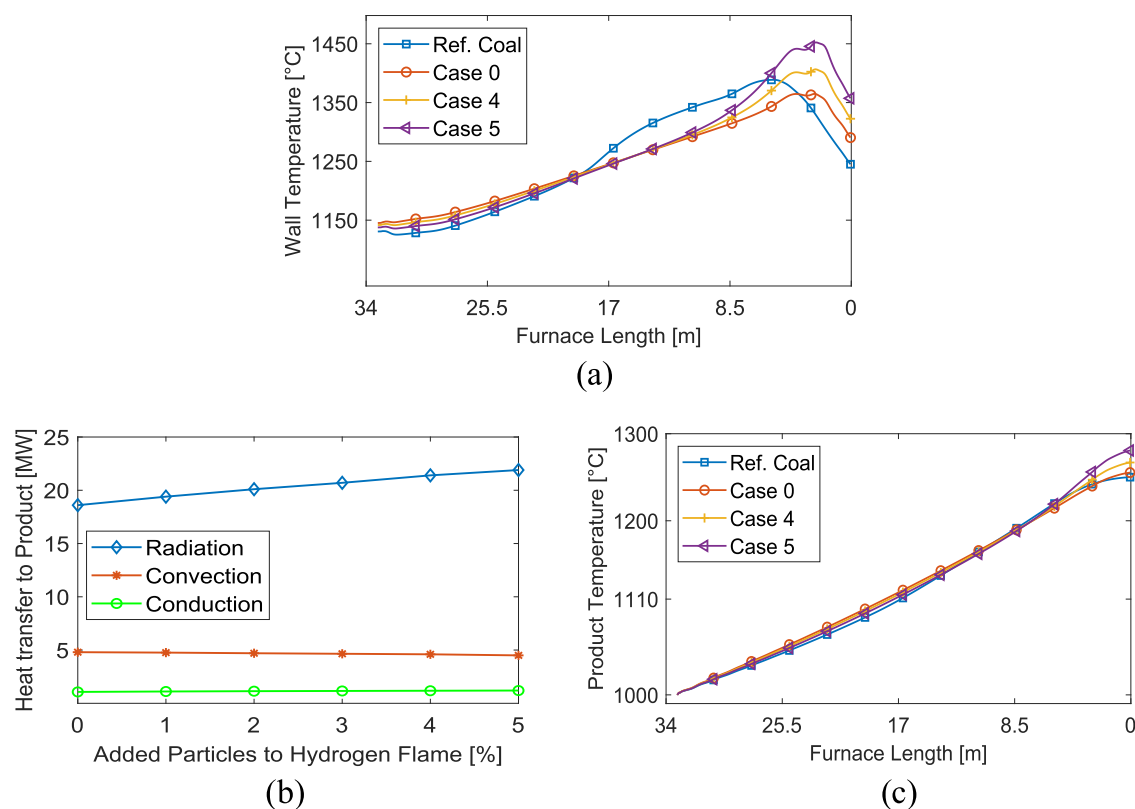
(a)

(b)

(c)

Figure 11. (a) Kiln wall temperature for the reference and Cases 0, 4, and 5. (b) Radiative, (blue diamonds), convective, (red asterixis), and conductive (green rings) heat transfer to the product as a function of the fraction of added particles (relative to the reference coal flame) to the 5.4 m hydrogen flame. (c) Calculated product bed temperature for the reference, Cases 0, 4, and 5.

is required to fully understand the effects of switching fuels in the kiln.

5. CONCLUSIONS

The heat transfer characteristics during conditions relevant for hydrogen and coal firing in rotary kilns for iron ore pellets production have been analyzed in a modeling study. Important characteristics, such as flame lengths, temperature, gas, and particle concentration profiles representative of each fuel and firing condition, were analyzed using simplifying assumptions. These assumptions, particularly the applied gas temperatures in the kiln and close to the kiln wall, may favor the heat transfer conditions for the hydrogen flame.

Hydrogen firing is associated with shorter flames with higher gas temperature, relative to the reference coal flame. The pure hydrogen flames will also exclude combustion particles (char, ash, and soot particles). Relative to coal, the pure hydrogen flame has a decreased radiative heat transfer but may achieve similar total heat transfer to the product bed material due to the high convective heat transfer (depending on the boundary condition of the gas temperature distribution in the cells close to the kiln surfaces). Despite extreme variations between hydrogen and coal firing conditions, the result of this study indicates inertia in the material and kiln wall that facilitates the fuel shifts. Furthermore, the heat transfer to the inner kiln wall increases in the near-burner region by the high gas temperatures of the hydrogen flames, while it is reduced at 4−18 m from the fuel inlet due to the decreased particle load. Increasing the flame length increases the volume of hot gases, enhancing the total heat transfer to the kiln wall to give higher local kiln wall temperatures at a position 8 m from the

fuel inlet. The changed temperature distribution may affect production.

The addition of inert char particles to the hydrogen flame showed a modest change in radiative heat transfer to the product; however, it sharply increased heat transfer to the kiln wall in the near-burner regions. It was found that particle loads corresponding to 5% of the reference coal flame enhanced peak kiln wall temperatures by 9% in the near-burner region. Thus, a small concentration of particles in hydrogen firing has a substantial effect on the kiln wall, which is important to consider in co-firing operations.

■ ASSOCIATED CONTENT

ⓢ Supporting Information

The Supporting Information is available free of charge at https://pubs.acs.org/doi/10.1021/acs.iecr.3c02264.

> Data input of the carbon dioxide and the water vapor concentration for the reference coal flame, as well as the input of the temperature profile and the water vapor concentration for the pure hydrogen flame (Case 0) (PDF)

■ AUTHOR INFORMATION

Corresponding Author

Elias Ehlmé − *Chalmers University of Technology, Space, Earth and Environment, Göteborg SE-412 96, Sweden;* ⓘ orcid.org/0009-0002-3009-3554; Email: ehlme@ chalmers.se

Authors

Adrian Gunnarsson − *Chalmers University of Technology, Space, Earth and Environment, Göteborg SE-412 96, Sweden;* ● orcid.org/0000-0003-0352-948X

Klas Andersson − *Chalmers University of Technology, Space, Earth and Environment, Göteborg SE-412 96, Sweden;* ● orcid.org/0000-0001-5968-9082

Fredrik Normann − *Chalmers University of Technology, Space, Earth and Environment, Göteborg SE-412 96, Sweden*

Complete contact information is available at:
https://pubs.acs.org/10.1021/acs.iecr.3c02264

Notes

The authors declare no competing financial interest.

■ NOMENCLATURE

h enthalpy
h_{rxr} heat of reaction
I intensity
$\dot{m}$ mass flow
n cell number
Q heat transfer
R radius
$\hat{s}$ unit vector in a given direction
T temperature

■ GREEK SYMBOLS

κ absorption coefficient
σ_s scattering coefficient
Φ scattering phase function
Ω solid angle for in-scattering
λ air-to-fuel ratio

■ SUBSCRIPT

r   radial position
v   wavenumber
z   axial position

■ CHEMICAL COMPOUNDS

Fe_3O_4 magnetite
Fe_2O_3 hematite
O_2 oxygen

■ REFERENCES

(1) Jonsson, C. Y. C.; Stjernberg, J.; Wiinikka, H.; Lindblom, B.; Boström, D.; Öhman, M. Deposit formation in a grate-kiln plant for iron-ore pellet production. Part 1: Characterization of process gas particles. *Energy Fuels* **2013**, *27*, 6159−6170.

(2) Boateng, A. A. *Rotary Kilns Transport Phenomena and Transport Processes*; Butterworth-Heinemann: Burlington, 2008.

(3) Butler, B. W.; Denison, M. K.; Webb, B. W. Radiation heat transfer in a laboratory-scale, pulverized coal-fired reactor. *Exp. Therm. Fluid Sci.* **1994**, *9*, 69−79.

(4) Bäckström, D.; Johansson, R.; Andersson, K.; Wiinikka, H.; Fredriksson, C. On the use of alternative fuels in rotary kiln burners — An experimental and modelling study of the effect on the radiative heat transfer conditions. *Fuel Process. Technol.* **2015**, *138*, 210−220.

(5) Gunnarsson, A.; Bäckström, D.; Johansson, R.; Fredriksson, C.; Andersson, K. Radiative Heat Transfer Conditions in a Rotary Kiln Test Furnace Using Coal, Biomass, and Cofiring Burners. *Energy Fuels* **2017**, *31*, 7482−7492.

(6) Cross, M.; Young, R. W. Mathematical Model of Rotary Kilns Used in the Production of Iron Ore Pellets. *Ironmak. Steelmak.* **1976**, *3*, 129−137.

(7) Tscheng, S. H.; Watkinson, A. P. Convective heat transfer in a rotary kiln. *Can. J. Chem. Eng.* **1979**, *57*, 433−443.

(8) Herz, F.; Mitov, I.; Specht, E.; Stanev, R. Influence of the motion behavior on the contact heat transfer between the covered wall and solid bed in rotary kilns. In *Exp. Heat Transf.*; Taylor & Francis, 2015; Vol. *28*, No. 2, pp 174−188 DOI: 10.1080/08916152.2013.854283.

(9) Wes, G. W. J.; Drinkenburg, A. A. H.; Stemerding, S. Heat transfer in a horizontal rotary drum reactor. *Powder Technol.* **1976**, *13*, 185−192.

(10) Li, S.-Q.; Ma, L.-B.; Wan, W.; Yao, Q. A Mathematical Model of Heat Transfer in a Rotary Kiln Thermo-Reactor. *Chem. Eng. Technol.* **2005**, *28*, 1480−1489.

(11) Gorog, J. P.; Adams, T. N.; Brimacombe, J. K. Regenerative heat transfer in rotary kilns. *Metall. Trans. B* **1982**, *13*, 153−163.

(12) Krishnamoorthy, G.; Jimenez, M. Non-gray modeling of radiative heat transfer in hydrogen combustion scenarios. *Int. J. Energy Res.* **2012**, *36*, 789−797.

(13) Muthusamy, D.; Hansen, O. R.; Middha, P.; Royle, M. In *Modelling of Hydrogen Jet Fires Using Cfd*, 4th Int. Conf. Hydrog. Saf., 2011; p 5892.

(14) Mashhadimoslem, H.; Ghaemi, A.; Palacios, A.; Hossein Behroozi, A. A new method for comparison thermal radiation on large-scale hydrogen and propane jet fires based on experimental and computational studies. *Fuel* **2020**, *282*, No. 118864.

(15) Ilbas, M. The effect of thermal radiation and radiation models on hydrogen−hydrocarbon combustion modelling. *Int. J. Hydrogen Energy* **2005**, *30*, 1113−1126.

(16) Fan, X. hui.; Li, J.; Chen, X. ling.; Wang, Y.; Gan, M. Temperature Field Simulation Model for Rotary Kiln of Iron Ore Oxidized Pellet. *J. Iron Steel Res. Int.* **2013**, *20*, 16−19.

(17) Gunnarsson, A.; Andersson, K.; Adams, B. R.; Fredriksson, C. Full-scale 3D-modelling of the radiative heat transfer in rotary kilns with a present bed material. *Int. J. Heat Mass Transf.* **2020**, *147*, No. 118924.

(18) Gunnarsson, A.; Andersson, K.; Adams, B. R.; Fredriksson, C. Discrete-ordinates modelling of the radiative heat transfer in a pilot-scale rotary kiln. *Energies* **2020**, *13*, 2192.

(19) Forsmo, S. P. E.; Forsmo, S. -E.; Samskog, P. O.; Björkman, B. M. T. Mechanisms in oxidation and sintering of magnetite iron ore green pellets. *Powder Technol.* **2008**, *183*, 247−259.

(20) Modest, M. F. The Radiative Transfer Equation in Participating Media (RTE). In *Radiative Heat transfer*, 3rd ed.; Academic Press, 2013; pp 279−302 DOI: 10.1016/B978-0-12-386944-9.50010-8.

(21) Tsai, J. R.; Özişik, M. N. Radiation in cylindrical symmetry with anisotropic scattering and variable properties. *Int. J. Heat Mass Transf.* **1990**, *33*, 2651−2658.

(22) Johansson, R.; Leckner, B.; Andersson, K.; Johnsson, F. Account for variations in the H2O to CO2 molar ratio when modelling gaseous radiative heat transfer with the weighted-sum-of-grey-gases model. *Combust. Flame* **2011**, *158*, 893−901.

(23) Bordbar, H.; Fraga, G. C.; Hostikka, S. An extended weighted-sum-of-gray-gases model to account for all CO2 - H2O molar fraction ratios in thermal radiation. *Int. Commun. Heat Mass Transf.* **2020**, *110*, No. 104400.

(24) Charalampopoulos, T. T.; Chang, H. Determination of the wavelength dependence of refractive indices of flame soot. *R. Soc.* **1990**, *430*, 577−591.

(25) Foster, P. J.; Howarth, C. R. Optical constants of carbons and coals in the infrared. *Carbon* **1968**, *6*, 719−729.

(26) Lohi, A.; Wynnyckyj, J. R.; Rhodes, E. Spectral measurement of the complex refractive index of fly ashes of canadian lignite and sub-bituminous coals. *Can. J. Chem. Eng.* **2009**, *70*, 751−758.

(27) Gupta, R. P.; Wall, T. F. The optical properties of fly ash in coal fired furnaces. *Combust. Flame* **1985**, *61*, 145−151.

(28) Goodwin, D. G.; Mitchner, M. Flyash radiative properties and effects on radiative heat transfer in coal-fired systems. *Int. J. Heat Mass Transf.* **1989**, *32*, 627−638.

(29) Gunnarsson, A.; Simonsson, J.; Bäckström, D.; Mannazhi, N.; Bengtsson, P.-E.; Andersson, K. Radiative Heat Transfer Modeling and in Situ Diagnostics of Soot in an 80 kW th Propane Flame with Varying Feed-Gas Oxygen Concentration. *Proceeding os the Combstion institute* **2018**, *37*, 833−840.

(30) Wiinikka, H.; Sepman, A.; Ögren, Y.; Lindblom, B.; Nordin, L. O. Combustion Evaluation of Renewable Fuels for Iron-Ore Pellet Induration. *Energy Fuels* **2019**, *33*, 7819−7829.

🕮 Recommended by ACS

Laminar Burning Velocity Measurement of CH$_4$/NH$_3$/H$_2$–Air Premixed Flames under Engine Relevant Conditions

Pragya Berwal and Sudarshan Kumar

AUGUST 18, 2023
ENERGY & FUELS   READ ☑

Study on the Classification Performance of a Novel Wide-Neck Classifier

Yan Zheng, Hongzheng Zhu, *et al.*

AUGUST 15, 2023
ACS OMEGA   READ ☑

Performance Improvement of Biomass Cookstove: Insights from Computational Fluid Dynamics and Prototype Testing

Rahul Paramane, Jyeshtharaj Joshi, *et al.*

AUGUST 11, 2023
INDUSTRIAL & ENGINEERING CHEMISTRY RESEARCH   READ ☑

Explosive Characteristics and Kinetic Mechanism of Methane–Air Mixtures under High-Temperature Conditions

Yansong Zhang, Xiao Liu, *et al.*

JANUARY 19, 2023
ACS OMEGA   READ ☑

Get More Suggestions >